

Impact of Explicit Atmosphere–Ocean Coupling on MJO-Like Coherent Structures in Idealized Aquaplanet Simulations

WOJCIECH W. GRABOWSKI

National Center for Atmospheric Research, Boulder, Colorado

(Manuscript received 6 January 2005, in final form 16 December 2005)

ABSTRACT

This paper discusses the impact of the atmosphere–ocean coupling on the large-scale organization of tropical convection simulated by an idealized global model applying the Cloud-Resolving Convection Parameterization (CRCP; superparameterization). Because the organization resembles the Madden–Julian Oscillation (MJO), the results contribute to the debate concerning the role of atmosphere–ocean coupling in tropical intraseasonal oscillations.

The modeling setup is an aquaplanet with globally uniform mean sea surface temperature (SST) of 30°C (tropics everywhere) in radiative–convective quasi equilibrium. The simulations apply an interactive radiation transfer model and a slab ocean model with a fixed oceanic mixed layer depth. Results from several 80- and 100-day-long simulations are discussed, where the only difference between the simulations is the prescribed oceanic mixed layer depth, which varied from 5 to 45 m. A simulation with a very deep oceanic mixed layer is also performed to represent constant-SST conditions. The simulations demonstrate that the interactive SST impedes the development of large-scale organization and has insignificant impact on the dynamics of mature MJO-like systems. The impediment is the result of a negative feedback between the large-scale organization of convection and SST, the convection–SST feedback. In this feedback, SST increases in regions of already suppressed convection and decreases in regions with enhanced convection, thus hindering the large-scale organization. Once developed, however, the MJO-like systems are equally strong in interactive and constant-SST simulations, and compare favorably with the observed MJO.

The above impacts of the atmosphere–ocean coupling contradict the majority of previous studies using traditional general circulation models, where, typically, an enhancement of the intraseasonal signal occurs compared to prescribed-SST simulations. An explanation of this discrepancy is suggested.

1. Introduction

This paper contributes to the debate concerning the role of atmosphere–ocean coupling in intraseasonal oscillations in general, and in the Madden–Julian Oscillation (MJO; Madden and Julian 1971, 1994) in particular [see Zhang (2005) for a recent review of the MJO]. From the observational standpoint, there is little doubt that the atmospheric MJO leaves a distinct footprint on the upper ocean. Perhaps the most convincing evidence came from observations collected over the tropical western Pacific warm pool in the Tropical Ocean Global Atmosphere Coupled Ocean–Atmosphere Response Experiment (TOGA COARE; Webster and Lukas 1992). During the period between November 1992 and

February 1993, the passage of two strong MJOs over the observational network was documented (e.g., Anderson et al. 1996; Lin and Johnson 1996). These data were subsequently used to model atmospheric processes during the strongest event between early December and early January (Wu et al. 1998, 1999).

Traditional atmospheric general circulation models (GCMs) struggle with climate variability on intraseasonal time scales (e.g., Slingo et al. 1996; Lin et al. 2005). This discrepancy is not helped by the lack of a universal theory that accounts for tropical intraseasonal oscillations and the MJO. Mechanisms previously considered in the large-scale organization of tropical convection include coupling between convection and large-scale equatorial perturbations (e.g., Lindzen 1974; Chang and Lim 1988; Lau et al. 1989; Brown and Bretherton 1995; Chao and Deng 1998; Majda and Shefter 2001; Grabowski and Moncrieff 2001), impact of clouds and moisture on radiative transfer (e.g., Pier-

Corresponding author address: Wojciech W. Grabowski, NCAR/MMM, P.O. Box 3000, Boulder, CO 80307-3000.
E-mail: grabow@ncar.ucar.edu

rehumbert 1995; Nilsson and Emanuel 1999; Raymond 2000a; Raymond and Zeng 2000; Raymond 2001; Grabowski and Moncrieff 2002; Bony and Emanuel 2005), impact of free-tropospheric humidity on convection (e.g., Raymond 2000b; Tompkins 2001a,b; Grabowski 2003a; Grabowski and Moncrieff 2004; Bony and Emanuel 2005), impact of convectively generated gravity waves on subsequent convective development (e.g., Mapes 1993, 1998; Oouchi 1999), upscale effects of the mesoscale organization of convection (Moncrieff 2004) and synoptic-scale waves (Biello and Majda 2005), and the impact of atmosphere–ocean interaction. The theories concerning atmosphere–ocean interaction include two different mechanisms: (i) the impact of fluctuations of the surface wind on heat fluxes from the ocean to the atmosphere [wind-induced surface heat exchange (WISHE) Emanuel 1987; Neelin et al. 1987], and (ii) the coupled atmosphere–ocean dynamics, where variations of the sea surface temperature (SST) drive atmospheric variations, which in turn affect the spatial distribution of the SST (e.g., Flatau et al. 1997; Sperber et al. 1997; Stephens et al. 2004).

The majority of models where SST is allowed to vary on intraseasonal time scales (e.g., coupled atmosphere–ocean GCMs) improve climate variability on these time scales (e.g., Flatau et al. 1997; Waliser et al. 1999; Woolnough et al. 2001; Inness and Slingo 2003; Fu and Wang 2004; Zheng et al. 2004; Maloney and Sobel 2004), but no impact is observed in some models (e.g., Hendon 2000). Since it is observed that the SST changes in a specific way during the passage of the MJO, the basic question is the impact of SST changes on the atmosphere. Is the ocean merely responding to the evolving surface forcing, or, alternatively, is the atmospheric MJO enhanced by concurrent changes of the SST? If indeed interactive SST enhances the atmospheric MJO, this may explain the improvement of the MJO signal in the majority of coupled climate models. Unfortunately, model results discussed herein do not support such a conjecture.

This paper presents results from idealized simulations of intraseasonal oscillations on a constant-SST aquaplanet using the Cloud-Resolving Convection Parameterization (CRCP; superparameterization; Grabowski and Smolarkiewicz 1999). It extends modeling studies presented in Grabowski (2001, 2003a,b, 2004) and in Grabowski and Moncrieff (2004), where spontaneous development of MJO-like systems was simulated. Sensitivity simulations reported in Grabowski (2003a) shed light on mechanisms behind formation and maintenance of the MJO-like systems. Because the coherence develops in simulations applying either prescribed radiative cooling or an interactive radiation

transfer model, large-scale coupling between radiative transfer and atmospheric moisture (water vapor and clouds) is evidently not the key mechanism. By replacing spatially variable surface latent and sensible heat fluxes by their spatially uniform averaged values, it was shown that the WISHE mechanism aids development of the MJO-like system, but, once present, such system can survive even with horizontally uniform surface fluxes. As discussed in Grabowski (2003a) and further illustrated in Grabowski and Moncrieff (2004), the interaction between convection and the free-tropospheric humidity, the moisture–convection feedback, is a plausible mechanism for the development and maintenance of the MJO-like systems. In the large-scale moisture–convection feedback, spatial fluctuations of deep convection cause coherent perturbations of free-tropospheric moisture, which, in turn, affect the spatial distribution of deep convection. Interactive radiation strengthens the moisture–convection feedback because enhanced large-scale circulation results from differences in radiative cooling between areas with enhanced and suppressed convectively generated moisture and cloudiness (see discussion in Grabowski and Moncrieff 2002).

In this paper, previous simulations are extended by investigating the impact of explicit coupling between the atmosphere and the ocean on the development and maintenance of MJO-like systems. The next section describes the numerical model and provides basic information about the simulations. Model results are presented in sections 3 and 4, where the impact of the atmosphere–ocean coupling on, respectively, the development and the maintenance of large-scale organization of convection is investigated. Implications for intraseasonal oscillations in traditional climate models are discussed in section 5, and the paper concludes in section 6.

2. Model description and numerical simulations

The numerical setup is the same as in previous aquaplanet studies by this author using the superparameterization approach (e.g., Grabowski 2001, 2003a,b, 2004). The global model is the anelastic nonhydrostatic two-time-level nonoscillatory forward-in-time Eulerian model in spherical geometry (Smolarkiewicz et al. 2001; Grabowski and Smolarkiewicz 2002) applying a low horizontal resolution (32×16), with 51 levels in the vertical and a uniform vertical grid length of 0.5 km. The global model time step is 12 min. The two-dimensional (2D) anelastic cloud-scale model embedded in each column of the global model has periodic horizontal domain of 200 km with a 2-km grid length

and the same vertical grid as the global model. The cloud model time step is 20 s. The cloud-scale models are aligned along the mean wind in the lowest 4 km (i.e., cloud models have variable orientation) and include the surface drag. The latter was shown in Grabowski (2004) to reduce the surface large-scale flow (reaching speeds in excess of 30 m s^{-1} , e.g., Figs. 1, 2, and 4 in Grabowski 2003a) to levels consistent with the observed MJO. Thermodynamic fields and horizontal velocity components between large-scale and cloud-scale models are coupled at every large-scale model time step (cf. section 2b in Grabowski 2004).

The simulations apply an interactive radiation transfer model (Kiehl et al. 1994) within the cloud-scale model domains in the independent column approximation mode. The radiative transfer uses cloud-scale fields supplied by the cloud-scale model as in traditional cloud-resolving simulations (e.g., Wu et al. 1998, 1999) and does not involve any subgrid-scale assumptions concerning cloud structure and overlap. The diurnal cycle of solar radiation is not considered and the solar constant is reduced to 436 W m^{-2} (i.e., the nominal solar constant at an equinox divided by π). A zero zenith angle is assumed over the entire aquaplanet. Although highly idealized, this setup is consistent with the “tropics everywhere” design of aquaplanet simulations. The radiative calculations are performed once every global model time step (i.e., every 12 min). The effective radius for cloud water droplets is assumed to be $10 \text{ }\mu\text{m}$, whereas for ice particles the effective radius depends on the ice water content based on measurements in tropical anvils reported by McFarquhar and Heymsfield (1997), see Eq. (2) in Grabowski (2000).

To investigate the impact of the atmosphere–ocean coupling, a simple slab ocean model is coupled to the cloud-scale model. However, for simplicity, cloud-scale fluctuations of the SST are not considered and a single value of the SST is predicted for each cloud-scale model (i.e., for each large-scale model column). The SST evolution is given by

$$\rho_w c_w D \frac{dT_s}{dt} = -\langle F_S \rangle - \langle F_L \rangle + \langle R^s \rangle - \langle R^l \rangle - Q, \quad (1)$$

where T_s is the slab ocean temperature; $\rho_w = 10^3 \text{ kg m}^{-3}$ is the water density; $c_w = 4.3 \times 10^3 \text{ J kg}^{-1} \text{ K}^{-1}$ is the specific heat of water; D is the slab ocean depth (assumed constant, see below); $\langle \cdot \rangle$ represents the horizontal average of small-scale model variables; F_S and F_L are surface sensible and latent heat fluxes; R^s and R^l are the net shortwave and net longwave radiative fluxes at the ocean surface; and Q is the heat loss due to

processes neglected in the model. In simulations described here, the “ Q flux” ensures that the slab ocean temperature averaged over each latitude is equal to the value applied in previous constant-SST simulations (30°C). Typical values for the Q flux are between 50 and 100 W m^{-2} , consistent with the tropics-everywhere modeling setup, which neglects heat transport (in the ocean and in the atmosphere) from Tropics to extratropics in the earth’s climate system. Note that T_s predicted by (1), and the corresponding saturated water vapor mixing ratio at the surface, are used to calculate spatially variable sensible and latent heat fluxes from the ocean into the atmosphere. In other words, the model does allow for small-scale variability of the surface fluxes, but not the SST. In the rest of the paper, we will refer to T_s as either SST or the slab ocean temperature.

Several 80- and 100-day-long simulations are performed, all starting from the large-scale atmosphere at rest with randomly distributed deep convection, in the spirit of previous constant-SST simulations (e.g., Grabowski 2001, 2003a,b, 2004). The only difference between the simulations is the assumed slab ocean depth, with values of 5, 10, 15, 25, 45, and $1.5 \times 10^4 \text{ m}$. The slab ocean depth $D = 15 \text{ m}$ corresponds to the averaged depth of the density-based oceanic mixed layer during TOGA COARE (see Table 4 in Anderson et al. 1996). The SST in simulation with $D = 1.5 \times 10^4 \text{ m}$ is for all practical purposes constant and equal to 30°C (this simulation will be referred to as constant SST). Simulations with depth of 5, 10, 15, 25, and 45 will be referred to as, respectively, D5, D10, D15, D25, and D45 in the following discussion.

3. Development of the large-scale organization

a. Simulation results

Figures 1, 2, and 3 illustrate development of eastward-propagating large-scale coherences near the equator in simulations D5, D15, and the constant SST. Simulations with other depths of the mixed layer model are similar to those highlighted in the three figures and are not shown. In general, the development of large-scale organization is similar to the early stages of previous simulations (cf. Figs. 1, 2, and 5 in Grabowski 2003a; Figs. 1 and 2 in Grabowski 2003b; Figs. 1, 4, and 7 in Grabowski 2004). The results shown in Figs. 1 to 3 have several features in common; such as the eastward propagation of developing coherences, the maximum surface precipitation over areas with the large-scale ascent, the low-level westerlies and upper-level easterlies to the west of the maximum surface precipitation, and

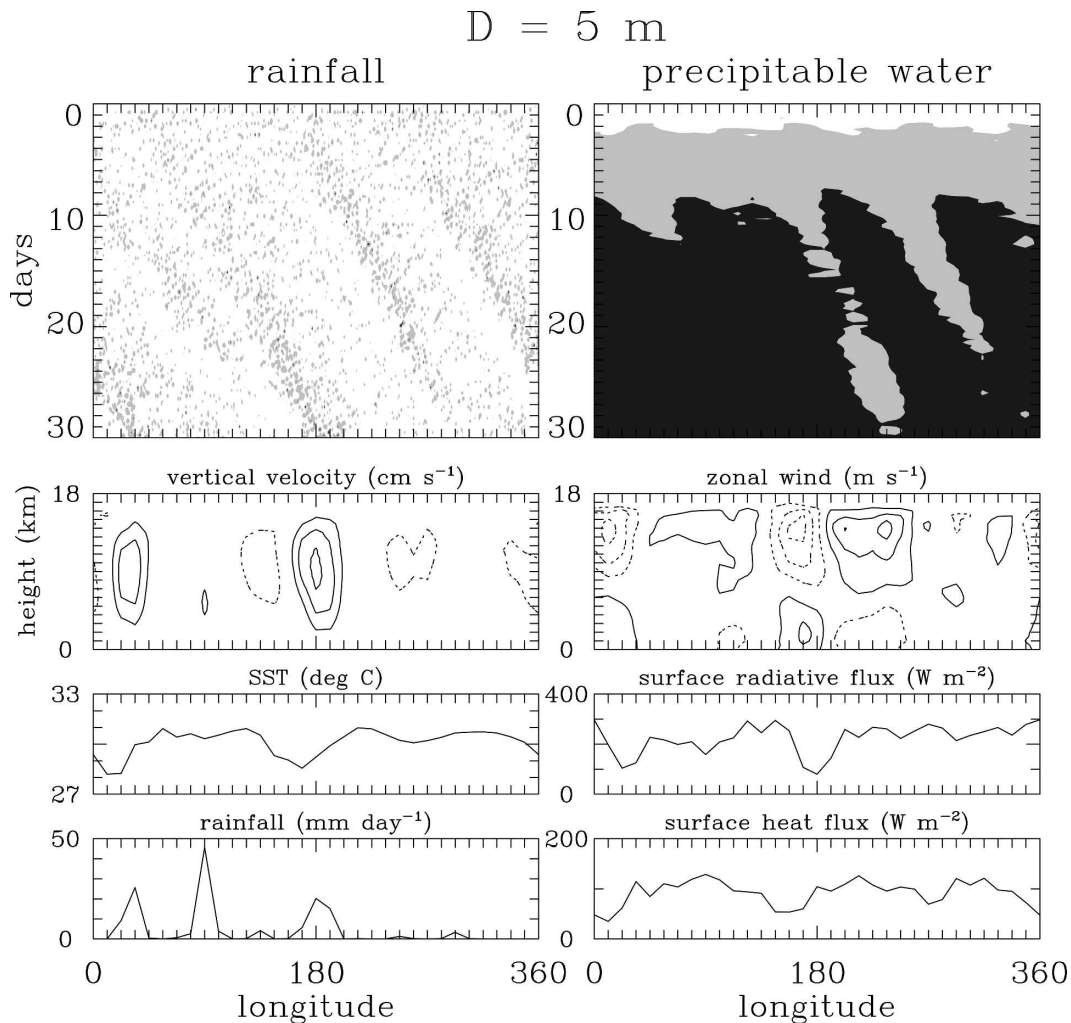
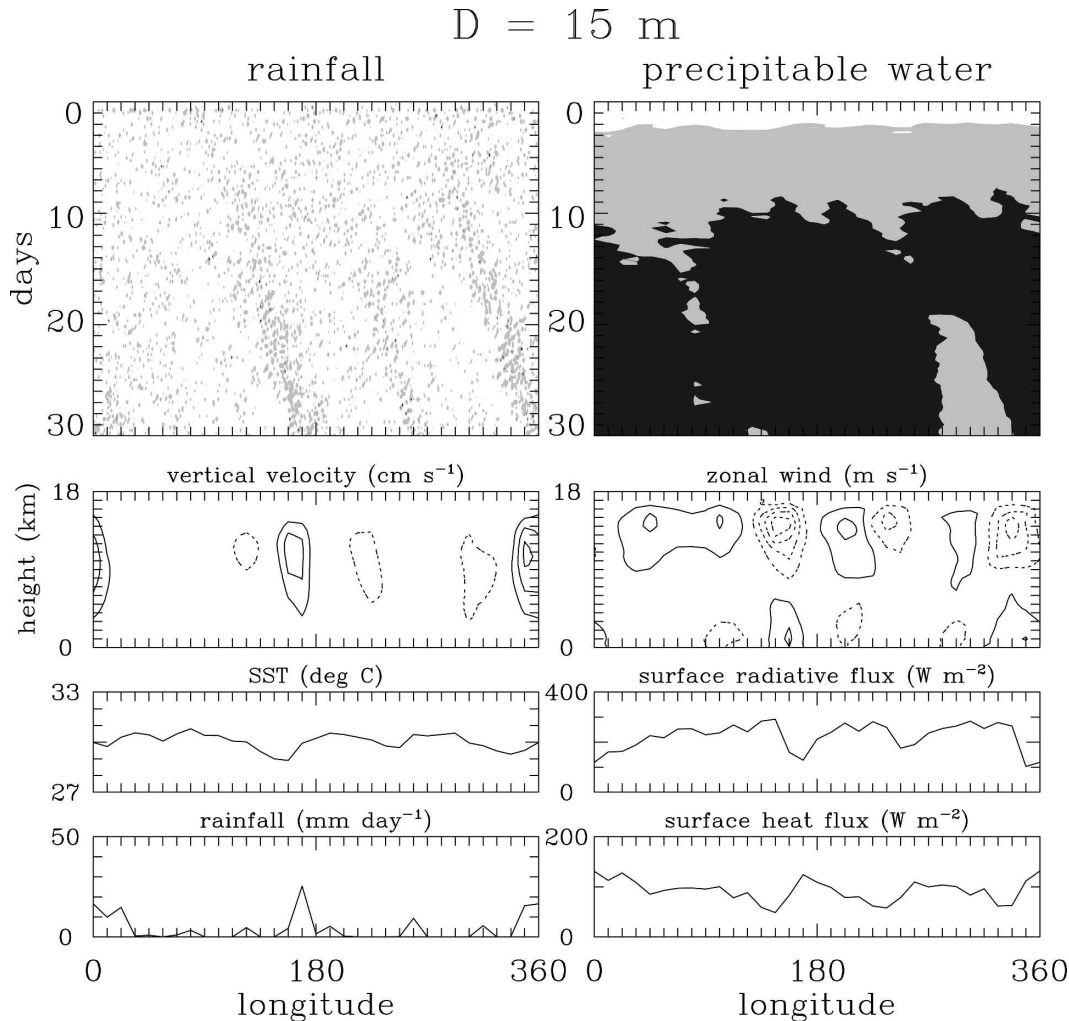


FIG. 1. Results from the simulation with $D = 5 \text{ m}$. Hovmöller diagrams of the (upper left) surface precipitation and (upper right) precipitable water at the equator. Precipitation intensities smaller (larger) than 0.2 (5) mm h^{-1} are shown using white (black) shading; gray shading represents precipitation intensities between 0.2 and 5 mm h^{-1} . Precipitable water smaller (larger) than 73 (82) kg m^{-2} is shown as white (black); gray shading is for precipitable water between 73 and 82 kg m^{-2} . The two panels beneath the Hovmöller diagrams show (middle left) vertical and (middle right) zonal velocities in the vertical plane at the equator at day 30. Contour interval is 0.5 cm s^{-1} (3 m s^{-1}) for vertical (zonal) velocities starting at 0.5 cm s^{-1} (2 m s^{-1}); solid (dashed) contours are for positive (negative) values. (lower four) Spatial distributions of the SST, the net radiative flux into the ocean, the precipitation rate, and the sum of surface sensible and latent heat fluxes out of the ocean, all along the equator at day 30.

the region of the maximum surface precipitation coincident with the smallest surface radiative flux into the ocean and the largest heat flux out of the ocean. The figures also highlight differences between the simulations. First, the large-scale coherences develop faster in constant-SST simulation than in D5 and D15. This is apparent from the magnitude of velocity perturbations and the spatial variability of precipitable water, and will be quantified momentarily. Second, developing perturbations propagate faster when the mixed layer depth is smaller and this pattern is consistent throughout all the

simulations (not shown). This aspect will be explained in the next section. Finally, the maximum surface precipitation in simulations D5 and D15 (as well as in all other simulations with variable SST) tends to be located between the SST extrema, with the SST maximum to the east and the minimum to the west. Such an alignment is consistent with the eastward propagation of the coherences and the spatial distribution of surface radiative and heat fluxes. It is also consistent with alignment in realistic coupled climate model simulations (e.g., Waliser et al. 1999; Maloney and Sobel 2004) as

FIG. 2. As in Fig. 1, but for $D = 15 \text{ m}$.

well as in observations (e.g., Woolnough et al. 2000; Stephens et al. 2004).

The development of SST fluctuations is illustrated in Fig. 4, which shows the evolution of the equatorial maximum and minimum SST for the initial 30 days of the simulations. The figure shows that the range between the maximum and minimum SST gradually increases as the large-scale perturbations of convection and cloudiness develop. As expected, the rate of increase is largest for the smallest depth of the ocean, consistent with a small thermal inertia of the shallow ocean. The range reached at day 30, from about 0.7°C for D45 to 5°C for D5, is representative for the SST range at later times (not shown).

The surprising result that the large-scale coherences develop more rapidly in the constant-SST simulation is further quantified in Fig. 5. The figure shows the mean large-scale kinetic energy (LSKE) within the equatorial

waveguide (cf. Figs. 6 and 9 in Grabowski and Moncrieff 2004) for all simulations discussed in this paper. Mean LSKE is defined as $(1/V)\int \rho(u^2 + v^2 + w^2) dV$, where u , v , and w are global model velocity components, and ρ is the air density. The integration is over the troposphere within two longitudinal belts near the equator, and V is the integration volume. As Fig. 5 documents, LSKE increases approximately exponentially during days 3 to 20 [i.e., $\text{LSKE} \sim \exp(2t/\tau)$], with the e -folding time τ for velocity varying between 10 and 30 days. Constant-SST simulation experiences the fastest growth rate. Although there is a considerable scatter, it is generally true that simulations with deeper mixed layer (i.e., thick lines in the figure) tend to have larger growth rate than the simulations with the shallow depth (thin lines).

The interpretation of results shown so far is that the development of large-scale coherences is hindered by

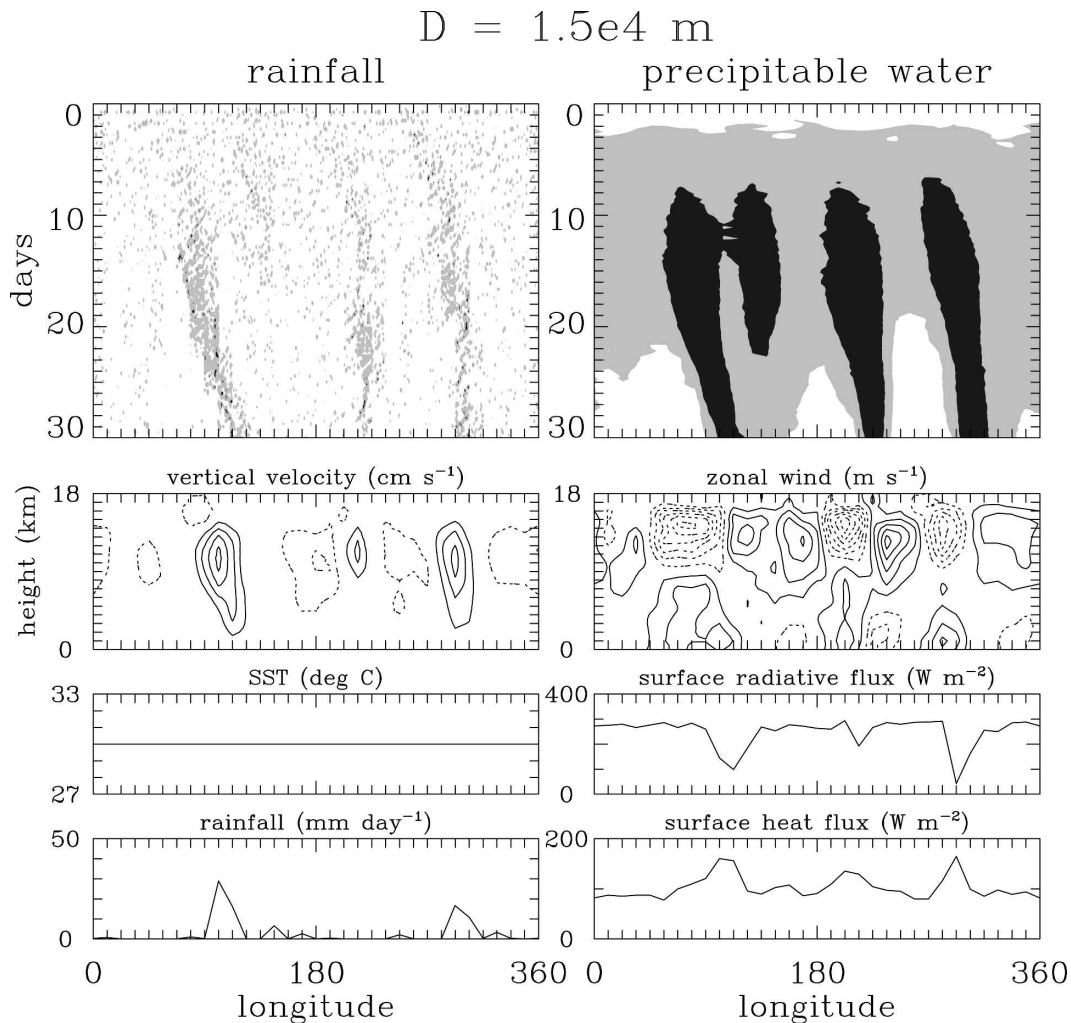


FIG. 3. As in Fig. 1, but for $D = 1.5 \times 10^4 \text{ m}$.

the interactive SSTs. The explanation involves two paradigms: the moisture–convection feedback (discussed in detail in Grabowski and Moncrieff 2004) and the convection–SST feedback, proposed in this paper. The two feedback mechanisms and their interaction are discussed in the next section.

b. Moisture–convection and convection–SST feedbacks

The moisture–convection feedback and the convection–SST feedback are schematically illustrated in Figs. 6 and 7, respectively. The figures illustrate interactions among convection, free-tropospheric humidity, and SST in a state of convective–radiative quasi equilibrium.

The moisture–convection feedback, discussed in detail in Grabowski and Moncrieff (2004), involves inter-

actions between deep convection and the free-tropospheric humidity. The upper panel of Fig. 6 shows a hypothetical situation where a positive moisture perturbation is introduced in the free troposphere in the center of the domain. This has two notable effects: First, the entrainment of humid environmental air into convective clouds slows the loss of positive buoyancy in updrafts compared to the scenario where drier environmental air gets entrained. Consequently, a larger fraction of clouds reaches the upper troposphere in the center of the domain as schematically illustrated. Second, precipitation falling outside clouds evaporates less efficiently when the environmental humidity is comparatively high. These two effects strengthen convective heating in the moister environment compared to the drier part of the domain.

In convective–radiative quasi equilibrium, large-scale

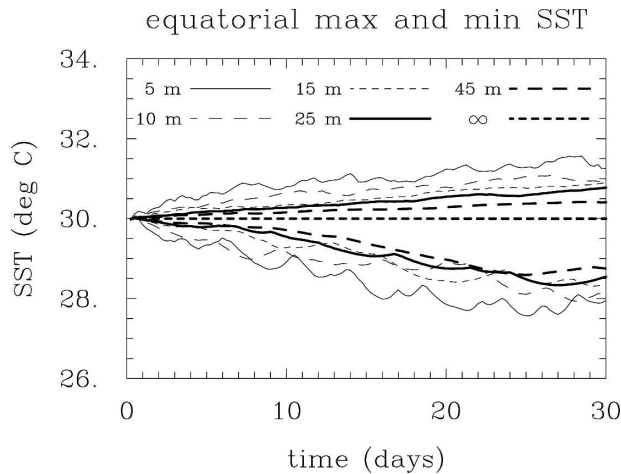


FIG. 4. Evolution of the equatorial maximum and minimum SST in all simulations.

differences in convective heating must be balanced by the temperature tendency due to an induced large-scale circulation. Because of the weak horizontal temperature gradients in the Tropics, the large-scale temperature advection is dominated by the vertical motion. Therefore an enhanced large-scale subsidence (illustrated by thick arrows remote from the center of the domain) develops in the area with suppressed convection. The key point is that the large-scale temperature homogenizes rapidly through the gravity wave mecha-

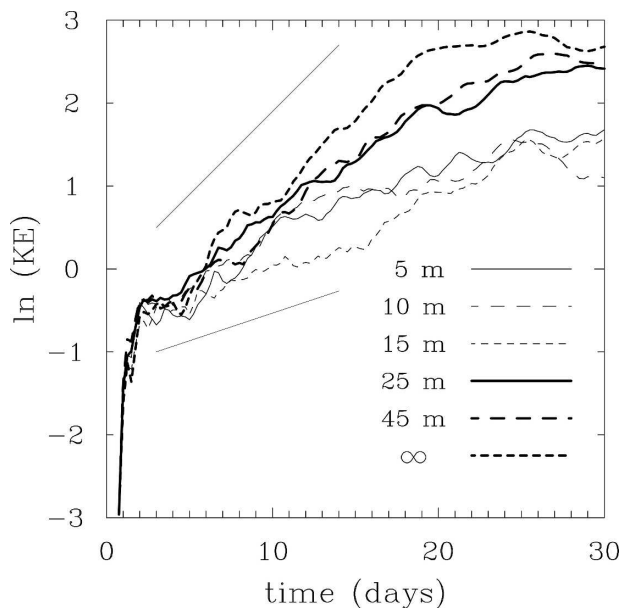


FIG. 5. Evolution of the tropospheric LSKE near the equator in all simulations. Growth corresponding to the 30- and 10-day e -folding times for velocity perturbations are shown by thin straight lines.

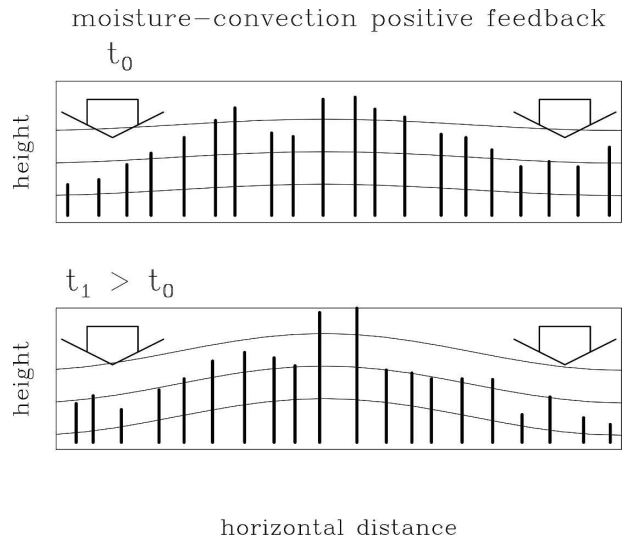


FIG. 6. Schematic representation of the moisture-convection feedback. Horizontal lines represent contours of water vapor mixing ratio and vertical thick lines mark convective clouds at different stages of their development (upper) shortly after a positive large-scale moisture perturbation is added in the center of the domain and (lower) the situation at a later time.

nism within the Rossby radius of deformation (cf. Bretherton and Smolarkiewicz 1989; Mapes 1993, 1998; Grabowski et al. 2000), whereas moisture detrained from convective clouds is advected by the mean flow, an inefficient mechanism on large scales.

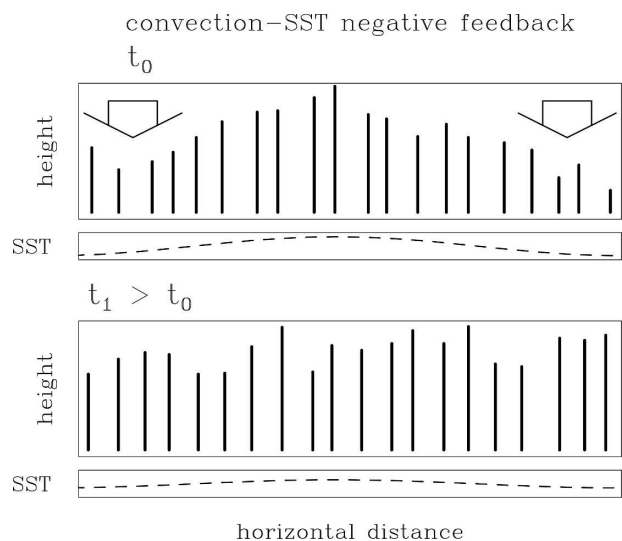


FIG. 7. Schematic representation of the convection-SST feedback. Vertical thick lines represent convective clouds at different stages of their development and SST distribution is shown beneath. (upper) Shortly after a positive large-scale SST perturbation is added in the center of the domain, and (lower) at a later time.

As time progresses (lower panel in Fig. 6), the large-scale gradient of free-tropospheric moisture strengthens as the middle and upper troposphere in the area with suppressed convection progressively experiences subsidence drying. In the center of the domain, on the other hand, the large-scale circulation maintains deep convection, which moistens the middle and upper troposphere. Moreover, the large-scale circulation and enhanced deep convection in the middle of the domain affect spatial distribution of surface fluxes (they increase toward the center of the domain; see Grabowski et al. 2000); these provides additional positive WISHE-like feedback. Furthermore, because of the impact of water vapor and clouds on radiative transfer, radiative cooling progressively weakens in the center of the domain compared to in the area with suppressed convection (e.g., Pierrehumbert 1995; Grabowski and Moncrieff 2002; Bony and Emanuel 2005). This accelerates the feedback even further.

Grabowski and Moncrieff (2004) estimated the time scale τ_{mcf} of the moisture–convection feedback to be of the order of the time scale characterizing the change of the free-tropospheric humidity in convective–radiative quasi equilibrium. Because this time scale is relatively long (of the order of 10 days), they argued that the moisture–convection feedback operates efficiently on intraseasonal time scales. Eliminating this feedback (by artificially removing large-scale heterogeneity of the free-tropospheric humidity) prevented MJO-like systems from developing, and—if already present—disintegrated them rapidly. Moreover, in simulations applying a conventional convection scheme (the Emanuel scheme), MJO-like systems were significantly enhanced when the Emanuel convection scheme was modified to make it more sensitive to the environmental humidity (see section 4 in Grabowski and Moncrieff 2004).

Figure 7 schematically illustrates the essence of the convection–SST feedback. In the upper panel, SST is higher in the center of the domain. Because of this, the large-scale circulation develops, with low-level flow along the SST gradient, reverse flow aloft, and ascent (subsidence) over highest (lowest) SSTs (see, e.g., Grabowski et al. 2000, and references therein). The large-scale subsidence associated with this circulation is shown by big arrows. Because of the subsidence, convection is suppressed over colder SSTs as schematically shown in the upper panel. As a result, the amount of solar radiation reaching the surface over cold SSTs increases compared to the warm SSTs. Moreover, stronger convection over warm SSTs enhances surface heat fluxes from the ocean into the atmosphere. These two effects result in the increase/decrease of SST over cold/

warm SSTs; that is, the initial SST perturbation is damped, as illustrated in the lower panel.

The time scale τ_{csf} of the negative convection–SST feedback can be estimated in a similar manner as for the moisture–convection feedback. For the moisture–convection feedback, the time scale was assumed to be of the order of the time scale of the free-tropospheric humidity change [cf. Eq. (1) in Grabowski and Moncrieff 2004]. For the convection–SST feedback, the time scale is assumed to be similar to the time scale of the SST change, namely,

$$\frac{1}{\tau_{\text{csf}}} \sim \frac{1}{\Delta T_s} \frac{dT_s}{dt}, \quad (2)$$

where $\Delta T_s \approx 2$ K is the magnitude of the SST change and dT_s/dt is given by (1). Taking the net change of the surface fluxes between suppressed and perturbed conditions as 200 W m^{-2} [see Figs. 1 to 3, and TOGA COARE estimates shown in Fig. 3 of Anderson et al. (1996)], and the oceanic mixed layer depth as 15 m, the time scale predicted by (2) is 7 days. Thus, the time scale for the convection–SST feedback is similar to the time scale of the moisture–convection feedback, $\tau_{\text{mcf}} \approx \tau_{\text{csf}}$. It follows that the convection–SST feedback can effectively oppose the moisture–convection feedback. This explains why in Fig. 5 the large-scale kinetic energy develops more slowly when SST is allowed to vary than when it is fixed.

Development of the large-scale organization illustrated in Figs. 1, 2, and 3 suggests a simple way the coupled atmosphere–ocean system mitigates the adverse impact of the convection–SST feedback. The key is the propagation of large-scale coherences up the large-scale SST gradient at speeds that result in changes of atmospheric conditions in a given location on time scales similar to both τ_{mcf} and τ_{csf} . In such a situation, a region of enhanced convection plays cat-and-mouse with the upper ocean: while moving over the ocean, the region of enhanced convection extracts the energy from the ocean (but also screens the ocean from the solar radiation), allowing ocean warming ahead by suppressing the deep convection. This situation is schematically illustrated in Fig. 8, where the coupled atmosphere–ocean perturbation propagates to the east, toward the SST maximum located to the east of the maximum surface precipitation. Such an alignment is evident in perturbations shown in Figs. 1 to 3, and it also applies to the mature MJO-like systems discussed in the next section (see Figs. 12 and 16). It is also consistent with observed intraseasonal oscillations (e.g., Lin and Johnson 1996; Woolnough et al. 2000; Stephens et al. 2004).

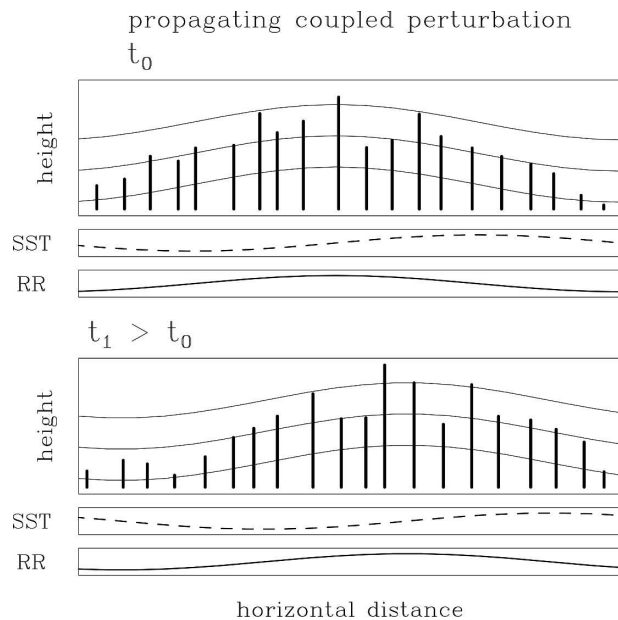


FIG. 8. Schematic representation of the interaction between the moisture–convection feedback and the convection–SST feedback resulting in the eastward-propagating coupled atmosphere–ocean perturbation. Horizontal lines represent contours of water vapor mixing ratio and vertical thick lines mark convective clouds at different stages of their development. Distributions of the SST and the surface rainfall rate (marked as RR in the figure) are shown beneath; perturbations at (upper) earlier and (lower) later times.

The cat-and-mouse mechanism illustrated in Fig. 8 was also evident in 2D cloud-resolving simulations without earth rotation reported in Grabowski (2000; see section 4 therein, Figs. 16 and 17 in particular). Therein, a slab ocean model (1) was coupled to the cloud-resolving model and the impact of cloud microphysics on the mean “climate” was investigated. These simulations featured a small periodic computational domain (1200 km). A shallow oceanic mixed layer depth of 2 m was selected purposely to accelerate the approach to the convective–radiative quasi equilibrium. Because of the small depth, the oceanic time scale (2) was about an order of magnitude shorter than in current simulations (except from D5 and D10) and allowed significant spatial SST variability (~ 1 K) even in the relatively small computational domain. Both the “westward” and “eastward” propagation (i.e., to the left and to the right in the 2D irrotational framework) occurred.

The reason why only eastward propagation occurs in the aquaplanet simulations herein concerns fundamental properties of the equatorial atmospheric wave dynamics, such as differences between eastward-propagating Kelvin waves and westward-propagating Rossby waves. As documented in Tompkins (2001a,b),

propagation of convection up the SST gradient in the absence of large-scale coherence is relatively slow (less than 1 m s^{-1}) and seemingly controlled by the rate of convective moistening of the free troposphere. In the case considered herein, however, the propagation of convective organization is most likely controlled by large-scale convectively coupled dynamics and it is considerably faster (e.g., around 5 m s^{-1} in Fig. 1).

The above discussion suggests a possible explanation of the difference in the propagation speed between developing perturbations in simulations with prescribed and interactive SST shown in Figs. 1 to 3. Because the simulations are initiated from the atmosphere at rest, developing large-scale perturbations tend to be stationary when SST is constant. This is in response to the moisture–convection feedback, additionally enhanced by the radiative forcing. Such stationary perturbations developed in idealized (2D, no rotation) cloud-resolving model simulations of Held et al. (1993) and Grabowski and Moncrieff (2002), and are consistent with theoretical predictions of Bony and Emanuel (2005). With the interactive ocean, on the other hand, the convection–SST feedback forces the large-scale perturbations to propagate to maintain the supply of energy from the ocean (the cat-and-mouse mechanism).

4. Mature MJO-like systems

The investigation of the impact of the atmosphere-ocean coupling on mature MJO-like coherences proved more complicated than initially thought. The reason is a gradual development of the mean large-scale meridional circulation between the equatorial waveguide and higher latitudes, which interferes with MJO-like coherences within the waveguide. This circulation is similar to the Hadley circulation on earth, but of the opposite sign (i.e., descent near the equator and ascent at higher latitudes; the counter-Hadley circulation). Arguably, the counter-Hadley circulation is associated with the differences between the large-scale organization of convection within and outside the waveguide. Its presence can be deduced from a weak meridional temperature gradient in simulations with prescribed radiation, see Fig. 12b in Grabowski (2001). This weak meridional temperature gradient is accompanied by a distinct meridional gradient of the relative humidity (see Fig. 12d therein). Except for the small virtual effect, the relative humidity gradient has insignificant impact when radiative cooling is prescribed. With interactive radiation, on the other hand, the counter-Hadley circulation strengthens in time because the meridional variability of column moisture feeds back on the radiative trans-

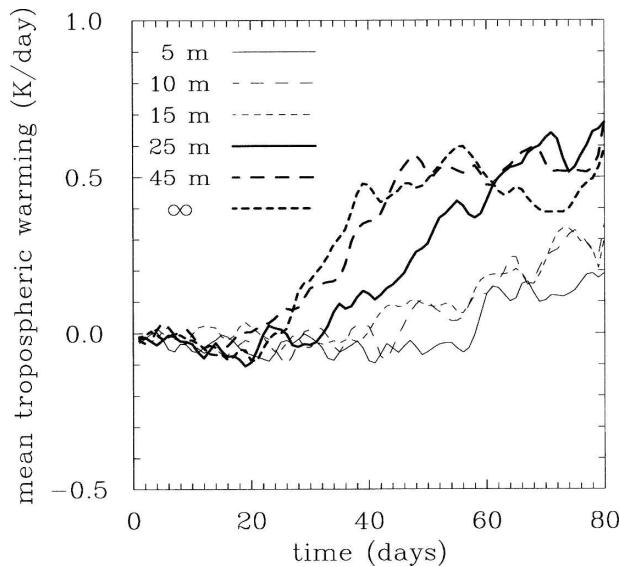


FIG. 9. Evolution of the mean tropospheric warming near the equator due to the counter-Hadley circulation in all simulations.

fer. This is the same mechanism that is argued by Raymond (2000a) to drive the Hadley circulation on earth.

The development of the counter-Hadley circulation in simulations with different depth of the oceanic mixed layer is illustrated in Fig. 9, which shows the mean tropospheric warming within the equatorial waveguide due to the mean meridional circulation. The warming is calculated as $-w(\partial\theta/\partial z)(T_e/\theta_e)$ (where w and θ are the vertical velocity and potential temperature fields in the global model, and T_e and θ_e are ambient temperature and potential temperature profiles) and averaged over two latitudinal belts adjacent to the equator and in the layer between the ocean surface and 16 km. The warming associated with the counter-Hadley circulation should be compared to a typical radiative cooling, which is around 1 K day^{-1} . As the figure shows, the effect of the counter-Hadley circulation is small for all simulations up to day 20. After that, the warming increases rapidly in the constant-SST simulation and more gradually in simulations D45 and D25. The counter-Hadley circulation develops later and even more gradually in simulation with shallow ocean. The key point is that it is difficult to compare large-scale organization of convection within the equatorial waveguide in various simulations beyond day 30 because the mean atmospheric cooling near the equator (i.e., the sum of radiative cooling and warming due to the counter-Hadley circulation) varies significantly.

To allow a fair comparison of mature MJO-like coherent structures, the counter-Hadley circulation should be the same in all simulations. The simplest solution is when the circulation is suppressed altogether

and this is the approach adopted here. To suppress the counter-Hadley circulation, global model equations for the temperature and the vertical and meridional velocity components are supplemented with a relaxation term damping the mean meridional circulation,

$$\frac{\partial\psi}{\partial t} = \dots - \frac{\bar{\psi} - \langle\psi\rangle}{\tau_{\text{rel}}}, \quad (3)$$

where ψ stands for θ , v , or w (i.e., the potential temperature, meridional, and vertical velocity); $\bar{\psi}$ is the zonal average of ψ at a given latitude and height; $\langle\psi\rangle$ is the global average at a given height; and τ_{rel} is the relaxation time scale. Short tests suggested that $\tau_{\text{rel}} = 1 \text{ h}$ is short enough to sufficiently damp counter-Hadley circulation (the mean warming is zero to within the thickness of the line when plotted in the same format as Fig. 9). It is important to note that (3) is applied to neither the zonal velocity component nor the moisture field, and that (3) does not affect perturbations of temperature and velocity components, but it only damps their mean meridional gradients.

Considering the range of SST variability in simulations discussed in the previous section, only three simulations were performed with the damping term, with $D = 15, 45$, and $1.5 \times 10^4 \text{ m}$. To reduce computational cost, they were restarted from day 20 of simulations described in the previous section. Figure 10 illustrates the evolution of surface precipitation and precipitable water near the equator in these simulations. The figure shows that all three simulations maintain the eastward-propagating coherences (typically two along the equator at a given time) for extended periods. The flow structure associated with these coherences (not shown) demonstrates that the pattern is indeed due to the MJO-like systems [cf. Figs. 4 and 5 in Moncrieff (2004), and accompanying discussion]. The propagation speed, similar in all simulations (typically between 4 and 5 m s^{-1}) fits MJO as well.

The next several figures illustrate the differences between the simulations with various depths of the oceanic mixed layer. A period between days 60 and 100 was selected for a detailed analysis of the atmosphere-ocean interactions during the passage of MJO-like systems. The model data for each simulation were averaged in the reference frame moving with the MJO-like systems, that is, with the speed of about 4.5 m s^{-1} (circumnavigation time of around 100 days), to obtain composite systems in each simulation.

Figures 11 and 12 present horizontal distribution of the surface precipitation, zonal wind, outgoing long-wave radiation (OLR), and SST perturbations for simulation with $D = 15$ and $1.5 \times 10^4 \text{ m}$. Results from the

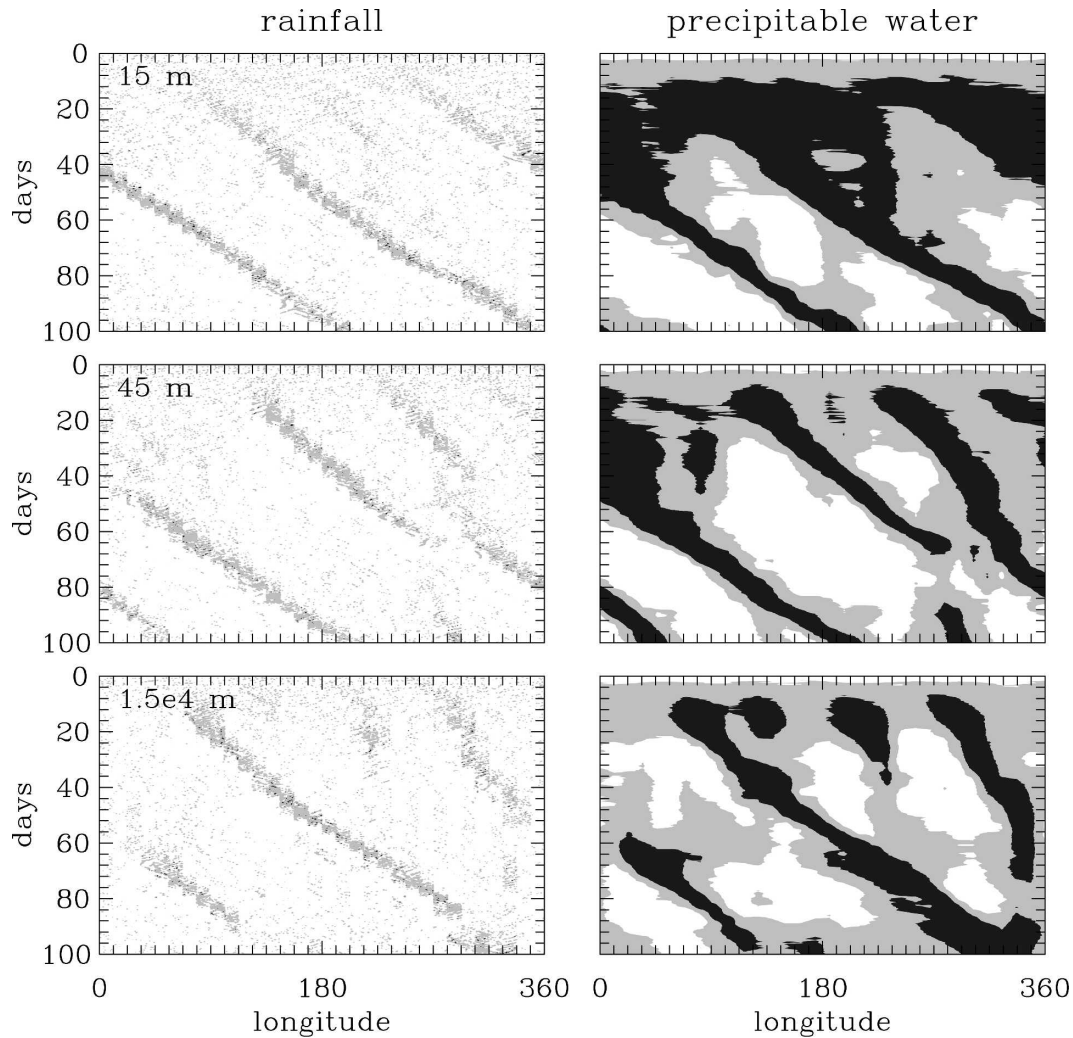


FIG. 10. Hovmöller diagrams of the (left) surface precipitation and (right) precipitable water at the equator for simulations with suppressed counter-Hadley circulation and oceanic mixed layer depth of (upper) 15 m, (middle) 45 m, and (lower) 1.5×10^4 m. Shading scheme as in Fig. 1.

third simulation ($D = 45$ m) are similar and are not shown. In general, the results are similar in the two simulations, both in terms of spatial patterns and the magnitudes, except for the SST perturbations, which vanish for the simulation with $D = 1.5 \times 10^4$ m (the amplitude of SST perturbations in $D = 15$ m simulation is about a half of those shown in Fig. 11). One can argue based on the data shown in the figures that the lower-tropospheric zonal winds behind the surface precipitation maxima (i.e., during the westerly wind bursts) are slightly stronger in the $D = 15$ m simulation than in $D = 1.5 \times 10^4$ m, but the opposite seems true for the OLR perturbations. In a nutshell, MJO-like coherences are similar regardless of the depth of the oceanic mixed layer.

One way to quantify the strength of MJO-like coher-

ences throughout the simulations is to consider temporal evolution of the mean westerly flow within the equatorial waveguide, the superrotation (cf. section 5d in Grabowski 2003a). As argued by Moncrieff (2004), the superrotation results from the impact of MJO-like coherent structures on the mean zonal momentum and thus it measures the integrated (i.e., time averaged) strength of MJO-like coherences. Superrotation was unrealistically strong in simulations without surface friction (5 to 10 m s^{-1} ; see section 5d in Grabowski 2003a), and was significantly reduced (down to between 2 and 4 m s^{-1}) when surface drag was included into the model physics (cf. Fig. 6 in Grabowski 2004). With surface friction, the strength of superrotation comes from a balance between meridional transport of zonal momentum by MJO-like coherences and frictional dissipa-

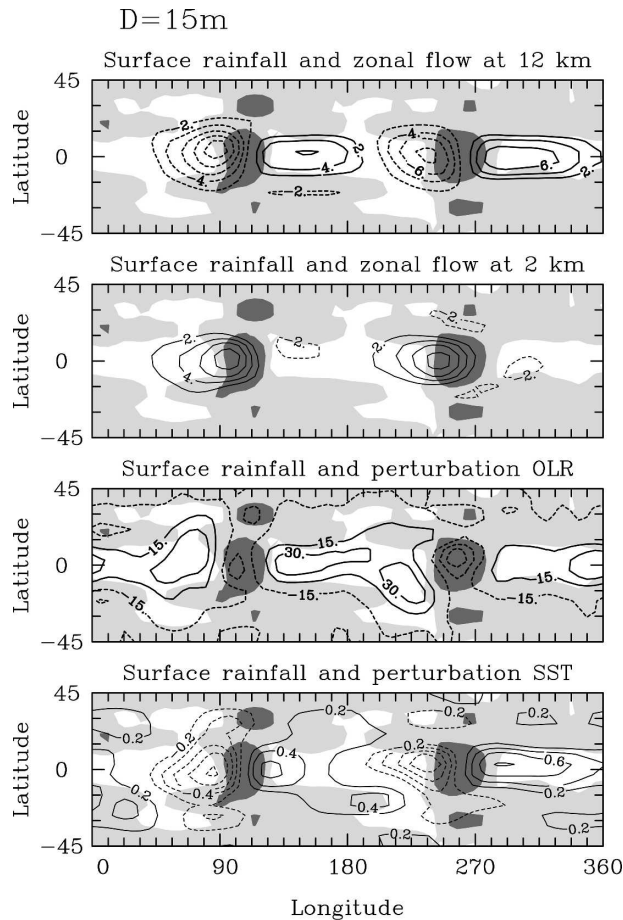


FIG. 11. Results from the simulation with oceanic mixed layer depth of 15 m. Horizontal distribution of the surface rainfall (grayscale) is shown in all panels. Precipitation intensities smaller (larger) than 2 (6) mm day^{-1} are shown using white (black) shading; gray shading is for intensities between 2 and 6 mm day^{-1} . Contours of zonal wind at height of (upper) 12 km and at (second from the top) 2 km, (third from top) OLR, and (bottom) SST perturbations. Contour interval for zonal winds is 2 m s^{-1} , with dashed contours representing negative values and zero contour omitted. Contour interval is 15 W m^{-2} for OLR and 0.2°C for the SST. Data are averaged for days 61 to 100 in the reference frame moving with the MJO-like systems (i.e., around 4.5 m s^{-1}).

tion. In three simulations discussed here, the evolution of the superrotation was similar after day 50, with 40-day averaged values (days 61–100) of 1.8 m s^{-1} for $D = 1.5 \times 10^4$ and 15 m, and 1.7 m s^{-1} for $D = 45$ m. This implies that the time-averaged strength of MJO-like coherences is the same in the three simulations.

Further analysis of the MJO-like coherences is presented in Figs. 13, 14, and 15. The figures show zonal distributions of various fields at the equator, averaged over days 61–100 in the moving reference frame as in Figs. 11 and 12, and centered at the position (or time) of the maximum surface precipitation. Since two MJO-

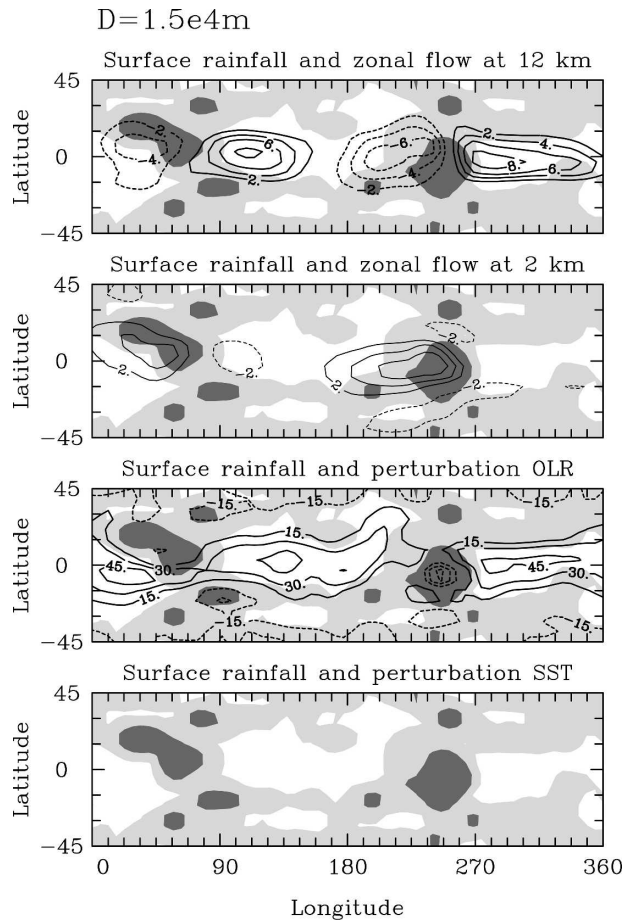


FIG. 12. As Fig. 11, but for simulation with oceanic mixed layer depth of 1.5×10^4 m.

like coherences are present for each simulation, the results are shown only in the vicinity of the stronger MJO-like coherent structure (i.e., the one featuring the larger maximum surface precipitation). The time scale shown at the bottom of the figures comes from converting zonal distance into time using the propagation speed of 4.5 m s^{-1} .

Figure 13 shows spatial-temporal distribution of the surface precipitation and OLR. Surface precipitation peaks at around 20 mm day^{-1} in all three simulations, which is similar to the budget estimates and model simulations for the period of the westerly flow onset during TOGA COARE that featured the largest surface precipitation (10 to 20 December; see Figs. 1, 5, and 6 in Wu et al. 1998). As expected, the maximum surface precipitation corresponds to the minimum OLR. The only noticeable difference between the simulations is the larger surface precipitation and lower OLR to the west of the peak precipitation in constant-SST simulation. The magnitude of the OLR variations,

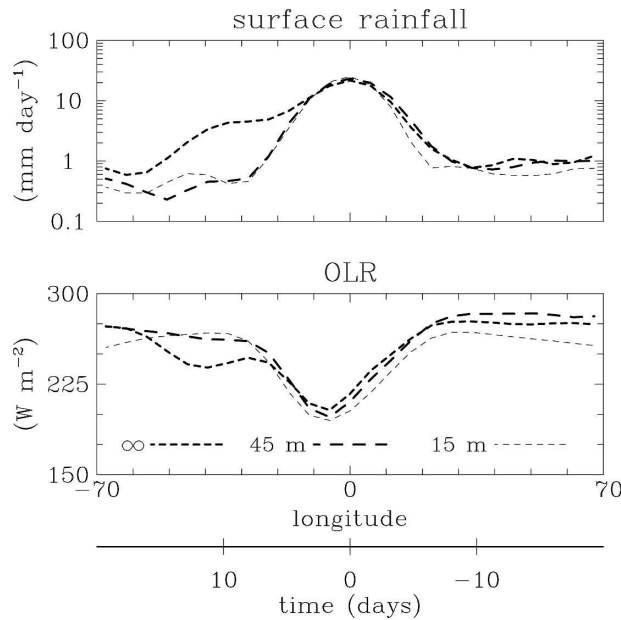


FIG. 13. Zonal-temporal distributions of surface rainfall and OLR at the equator obtained by averaging model results for days 61 to 100 in the reference frame moving with the MJO-like systems for simulations with oceanic mixed layer depth of 15, 45, and 1.5×10^4 m.

roughly from 280 to less than 200 W m^{-2} , is similar to the observations (cf. Fig. 13 in Wu et al. 1998). The OLR ahead of the maximum surface precipitation is larger than the one behind, which is due to more extensive upper-tropospheric cloudiness to the west of the maximum surface precipitation (not shown). This is likely the effect of stronger vertical shear of the zonal flow behind the maximum surface precipitation (cf. Figs. 11 and 12).

Figure 14 presents the distribution of the slab ocean temperature, surface heat flux (sensible plus latent), and surface zonal wind (relative to earth-stationary observer) in the same format as Fig. 13. Except for the SST evolution, the differences between the three simulations are minor. SST varies between 29.0° and 30.6°C when $D = 15$ m, and between 29.7° and 30.3°C when $D = 45$ m. As anticipated, the maxima/minima occur ahead/behind the maximum surface precipitation (e.g., Lin and Johnson 1996; Woolnough et al. 2000; Stephens et al. 2004). SST change during the simulated passage of the MJO-like coherence is comparable to the strongest event observed in TOGA COARE, where the SST changed from slightly above 30°C to slightly below 29°C between early December and early January (e.g., Fig. 4 in Weller and Anderson 1996; Fig. 1 in Wu et al. 1998). Some differences between model and observations are expected because of the simplifications of the

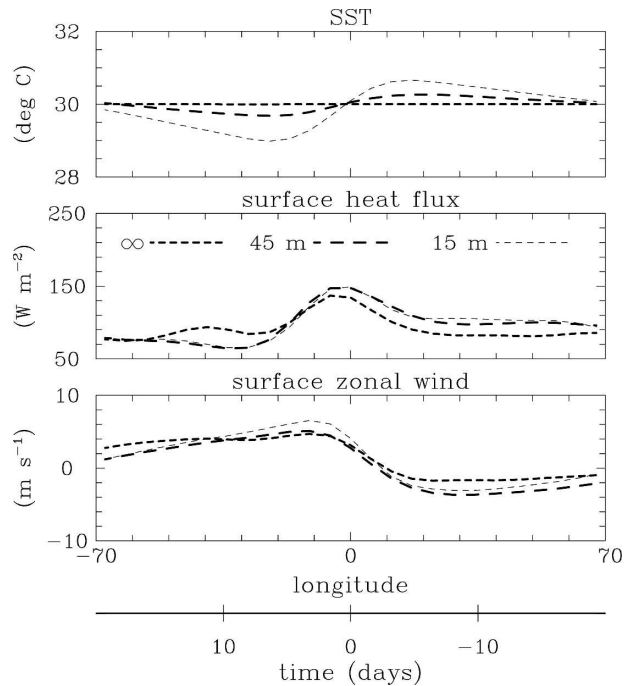


FIG. 14. As in Fig. 13, but for the SST, surface heat flux, and zonal wind at the ocean surface.

slab ocean model. For instance, the model does not consider variations of the mixed layer depth, which is observed to be larger during the westerly wind burst and smaller in suppressed conditions (e.g., Anderson et al. 1996). The model also excludes the wavelength-

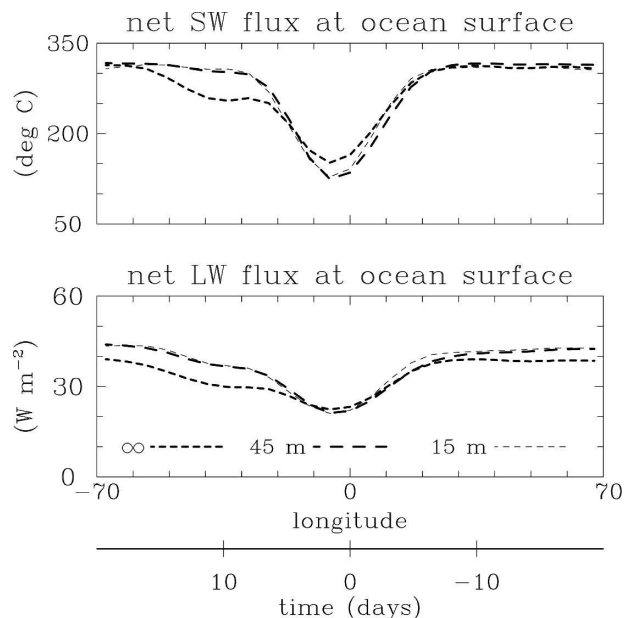


FIG. 15. As in Fig. 13, but for the net shortwave (SW) and longwave (LW) fluxes at the ocean surface.

dependent penetration of the solar radiation into the upper ocean. The maximum surface heat flux (around 200 W m^{-2}), in agreement with observations (see Figs. 10 and 11 of Wu et al. 1998), is shifted slightly westward from the maximum surface precipitation, so is the maximum surface westerly wind. In the observations, however, collocated maximum surface fluxes and surface winds are shifted more significantly toward the west of the maximum precipitation (e.g., Fig. 16 in Lin and Johnson 1996).

Figure 15 shows the spatial-temporal distribution of the net solar and longwave flux at the ocean surface. Again, the differences between the simulations are minor, perhaps with the exception of the area west of the maximum surface precipitation (see also Fig. 13). Figures 14 and 15 show that the rapid cooling of the ocean surface in simulations with variable SST is due to the combined effect of enhanced surface fluxes (an increase close to 100 W m^{-2}) and a reduction of the net solar flux into the ocean (a decrease of about 200 W m^{-2}). The changes of the net longwave flux at the surface are much smaller.

In summary, the results presented in Figs. 10 to 14 mimic many features of the real-world MJOs. Most importantly, the differences between simulations with constant and variable SST are minor and have only insignificant impact on the strength of the large-scale circulation.

5. Implications for intraseasonal oscillations in traditional GCMs

Modeling results discussed in sections 3 and 4 clearly demonstrate that, in the idealized setup of a “tropics everywhere” aquaplanet, atmosphere–ocean coupling impedes development of large-scale convective organization and it has insignificant impact on mature MJO-like system. These conclusions contradict results from the majority of traditional GCMs employed to investigate the earth’s climate, which typically demonstrate the enhancement of intraseasonal variability when coupled with the ocean model (see the introduction). In the context of intraseasonal oscillations in traditional GCMs, two separate issues need to be discussed. The first concerns the idealized nature of simulations discussed in this paper, and the second the deficiencies of intraseasonal variability in traditional climate models.

The idealized nature of simulations discussed in this paper is obvious, for example, absence of baroclinic effects associated with equator-to-pole surface temperature gradient and absence of continents. Moreover, the low spatial resolution of the global model results in a large gap of spatial scales, from largest scales resolved

in the cloud model (a hundred kilometers) to the shortest scales resolved by the global model (a few thousands of kilometers). This scale gap limits the types and scales of large-scale equatorially trapped perturbations supported by the model [for a review of convectively coupled disturbances observed in the Tropics, see Wheeler and Kiladis (1999) and Wheeler et al. (2000)]. All of the above aspects are likely relevant for the observed MJO. However, because SST fluctuations involve intraseasonal time scales, the impact of the atmosphere–ocean coupling on large-scale atmospheric dynamics in the Tropics simulated by our model is anticipated to be genuine.

Grabowski (2003a) argued that a plausible explanation for the low intraseasonal variability of the tropical convection in traditional climate models results from the lack of sensitivity of convective parameterizations to the free-tropospheric humidity, as documented in Derbyshire et al. (2004). Naturally, the moisture–convection feedback can operate only if a convective scheme employed is sensitive to environmental humidity. This was further illustrated in Grabowski and Moncrieff (2004) using the Emanuel convective scheme (Emanuel 1991). In its standard configuration, the Emanuel scheme is insensitive to free-tropospheric humidity (Derbyshire et al. 2004) and results in weak MJO-like systems in idealized aquaplanet simulations. However, enhancing the sensitivity artificially, by allowing more precipitation to fall outside convective clouds and thus be exposed to the environmental humidity, dramatically improves the simulated MJO-like systems [see Grabowski and Moncrieff (2004) for a detailed discussion].

In contrast to the moisture–convection feedback, the convection–SST feedback is relatively easy to capture using traditional convective parameterizations. This is because the enhanced/suppressed surface insolation in regions of suppressed/enhanced convection, the key element of this feedback, should operate even when simple convective and cloud schemes are applied. It follows that a plausible explanation of the impact of the atmosphere–ocean coupling on the intraseasonal oscillations in traditional climate models may stem from the weakness of the moisture–convection feedback and the strength of the convection–SST feedback. In such a situation, in agreement with the discussion in Grabowski and Moncrieff (2004), the intraseasonal oscillations would be weak because of the suppression of the moisture–convection feedback. With an interactive SST, on the other hand, the convection–SST feedback will likely induce propagating intraseasonal time-scale coupled perturbations, in line with the cat-and-mouse mechanism discussed in section 3b (cf. Fig. 8). As a

result, an enhancement of intraseasonal oscillations is to be expected compared to a constant-SST simulation. However, these oscillations should be weaker than in observations even in coupled simulations because no impact of the coupling is anticipated in strong MJO-like coherences as illustrated in section 4. This is supported by results of some coupled models. For instance, Waliser et al. (1999) state that the coupling of an atmospheric GCM to a slab ocean model resulted in a change of SST due to the passage of the MJO by less than 0.3 K and led to changes of surface heat and radiative fluxes in the range of $10\text{--}25\text{ W m}^{-2}$. These are considerably smaller than values deduced from the observations, either from TOGA COARE referred to in section 4 or from the reanalysis data (Woolnough et al. 2000).

Additional support for the above conjecture comes from simulations of developing disturbances (i.e., similar to those discussed in section 3a), but with suppressed moisture–convection feedback (cf. section 5c in Grabowski 2003a; Grabowski and Moncrieff 2004). In these simulations, a relaxation term is added to the water vapor equation of the global model that relaxes the water vapor toward the value given locally by the globally averaged relative humidity and the local temperature.¹ The relaxation time scale is one day as in Grabowski and Moncrieff (2004), and the relaxation is only applied for model levels above 2 km. Unfortunately, relaxing the relative humidity field affects not only the moisture–convection feedback, but to some extent the convection–SST feedback as well. This is because the convection–SST feedback relies on the spatial variability of clouds, which are affected by the mean relative humidity. Simulations with $D = 15$ and 1.5×10^4 m are performed (i.e., the simulations with the slowest and the fastest growth of LSKE in Fig. 5). The development of large-scale organization in these simulations is similar to that shown in Figs. 2 and 3, but the large-scale perturbations are stronger in the variable SST simulation. This is illustrated in Fig. 16, which shows evolution of the LSKE in the same format as Fig. 5. In contrast to the results shown in Fig. 5, LSKE is larger in the simulation with variable SST, with the mean value for days 21 to 30 in $D = 15$ m almost twice as large as in the constant-SST simulation, which implies about 40% stronger winds. This suggests that stronger intraseasonal oscillations are expected in a

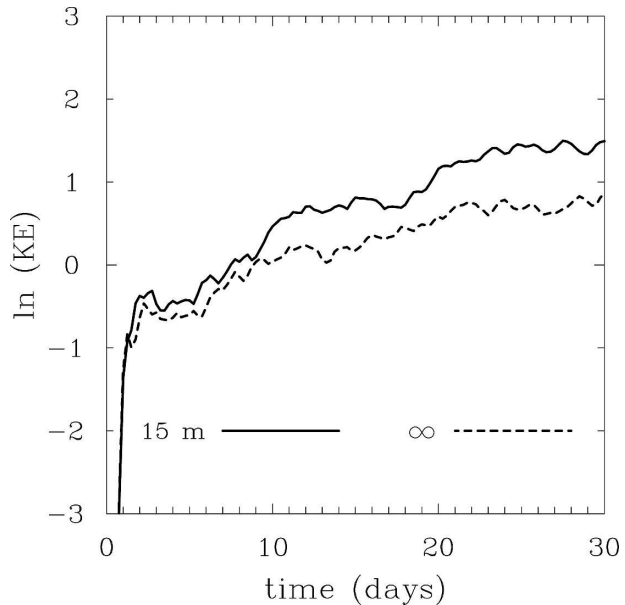


FIG. 16. Evolution of the tropospheric LSKE near the equator in simulations with the relaxation of the relative humidity using $D = 15$ and 1.5×10^4 m.

coupled model when the moisture–convection feedback is suppressed compared to the model with constant SSTs.

In summary, the impact of the atmosphere–ocean coupling on intraseasonal oscillations (the MJO in particular) in traditional climate models is argued to be consistent with the suppression of the moisture–convection feedback in those models and the presence of the convection–SST feedback, with the latter supporting propagating coupled atmosphere–ocean perturbations (the cat-and-mouse mechanism) characterized by intraseasonal time scales.

6. Concluding summary

This paper documented the impact of the atmosphere–ocean coupling on the development of large-scale convective organization and on the MJO-like systems simulated by a numerical model applying the Cloud-Resolving Convection Parameterization (the superparameterization). The idealized modeling setup was an aquaplanet with a globally uniform mean SST of 30°C (“tropics everywhere”), with the size and rotation of earth, in radiative–convective quasi equilibrium. This idealized problem was applied previously to investigate MJO-like systems (e.g., Grabowski 2003a, 2004). To simulate realistic changes of the ocean temperature, an interactive radiative transfer model was used together with a slab ocean model with fixed mixed layer depth.

¹ In Grabowski [2003a; cf. Eq. (1) therein] and Grabowski and Moncrieff (2004), water vapor mixing ratio was relaxed toward the global mean. Relaxing the relative humidity field is more appropriate when the SST varies.

The depth of the mixed layer was varied between 5 and 45 m in simulations with variable SST and it was given a large value (1.5×10^4 m) in simulations that mimic the constant-SST conditions.

Two sets of simulations were discussed. The first set started from $t = 0$, the large-scale atmosphere at rest, and with randomly distributed deep convection. The developing large-scale organization took the form of eastward-propagating convectively coupled disturbances, similar to previous simulations, and argued in Grabowski and Moncrieff (2004) to result from the moisture–convection feedback mechanism. This feedback involves spatial fluctuations of deep convection causing perturbations of the free-tropospheric humidity, which in turn affect the spatial distribution of deep convection (cf. Fig. 6). Grabowski and Moncrieff argued that the feedback involves relatively long time scales and is key to tropical intraseasonal oscillations.

Evolution of the large-scale kinetic energy associated with developing convectively coupled disturbances demonstrated that the interactive ocean impeded development of the large-scale organization. This was explained as the impact of the convection–SST feedback that partially negates the moisture–convection feedback. The convection–SST feedback (see Fig. 7) is a process by which SST perturbations in the Tropics are damped by deep convection. This is because deep convection tends to develop preferentially over warm SSTs, with the lower (higher) SST regions experiencing enhanced (suppressed) surface insolation and suppressed (enhanced) surface heat fluxes. These processes all tend to reduce SST perturbations on time scales comparable to the moisture–convection feedback. The fact that the convection–SST feedback opposes the moisture–convection feedback explains why the large-scale kinetic energy increases faster when SST is constant compared to when it is allowed to vary.

The coupled atmosphere–ocean system copes with the adverse impact of the convection–SST feedback by allowing coupled perturbations to propagate as illustrated in Fig. 8. In simulations discussed in this paper, the large-scale organization propagates toward the east, with higher (lower) SSTs located to the east (west) of the maximum surface precipitation that coincides with the large-scale ascent. For the optimum coupling between the atmosphere and the ocean, the propagation speed of coupled perturbations needs to be consistent with the intraseasonal time scales of the moisture–convection feedback in the atmosphere and the convection–SST feedback in the ocean, as well as with the horizontal scale of the large-scale organization. It follows that the pattern needs to propagate several thousands of kilometers in about 10 days, which is in the

range of 5 to 10 m s^{-1} . This is the range characterizing both developing convectively coupled perturbations and mature MJO-like systems in simulations discussed herein.

Because the first set of simulations featured not only development of large-scale perturbations discussed above, but also a mean meridional circulation between the equatorial waveguide and higher latitudes, the counter-Hadley circulation, the second set of simulations included an additional term in the temperature and the vertical and meridional momentum equations. This term eliminated the counter-Hadley circulation and allows a fair comparison of MJO-like coherences in simulations with various depth of the oceanic mixed layer. Considering the magnitude of SST fluctuations in the first set, only simulations with depth of 15, 45, and 1.5×10^4 m were performed. They were initiated from day 20 of corresponding simulations from the first set and run up to day 100. The main conclusion from the second set is that the interactive SST has virtually no effect on mature MJO-like coherences. This implies that the upper ocean merely responds to the atmospheric forcing, with a minimal feedback on atmospheric processes. This conclusion contradicts speculations that the MJO is a coupled mode of climate variability (cf. section 6 in Sperber et al. 1997; Stephens et al. 2004). It also contradicts most studies using traditional climate models, which typically show enhanced intraseasonal signal when coupled to the interactive ocean.² At the same time, the spatial distributions and the magnitudes of surface heat fluxes, surface precipitation, shortwave and longwave radiative fluxes, and the large-scale flow associated with MJO-like systems compared favorably with data collected during TOGA COARE over the tropical western Pacific.

This study offers limited insight as to why traditional climate models demonstrate a drastically different impact of the atmosphere–ocean coupling on the strength of intraseasonal oscillations. It is argued that such models simulate weak intraseasonal oscillations because of their inability to represent the moisture–convection feedback. As illustrated by an additional sensitivity experiments with suppressed moisture–convection feedback (cf. Fig. 16), this weak variability is enhanced when propagating coupled atmosphere–ocean perturbations with intraseasonal time scales are generated in response to the convection–SST feedback via the cat-and-mouse mechanism.

To evince the impact of the atmosphere–ocean cou-

² It should be kept in mind, however, that studies using traditional climate models draw their conclusions from a much larger sample of events.

pling on MJO on earth, realistic climate simulations using a superparameterization approach, similar to those discussed in Khairoutdinov et al. (2005), should be extended to include a slab ocean model. We hope results of such simulations will be reported in the future.

Acknowledgments. Comments on the manuscript by Mitch Moncrieff, Adam Sobel, Steve Woolnough, and two anonymous reviewers are acknowledged, as is the editing of the manuscript by Penny Warfel. Computer time was provided by NSF MRI Grants CNS-0421498, CNS-0420873, and CNS-0420985, NSF sponsorship of the National Center for Atmospheric Research and the University of Colorado, and a grant from the IBM Shared University Research program. NCAR is operated by the University Corporation for Atmospheric Research (UCAR) under sponsorship of the NSF.

REFERENCES

- Anderson, S. P., R. A. Weller, and R. Lukas, 1996: Surface buoyancy forcing and the mixed layer of the Western Pacific warm pool: Observations and 1D model results. *J. Climate*, **9**, 3056–3085.
- Biello, J. A., and A. J. Majda, 2005: A new multiscale model for the Madden–Julian Oscillation. *J. Atmos. Sci.*, **62**, 1694–1721.
- Bony, S., and K. A. Emanuel, 2005: On the role of moist processes in tropical intraseasonal variability: Cloud–radiation and moisture–convection feedbacks. *J. Atmos. Sci.*, **62**, 740–759.
- Bretherton, C. S., and P. K. Smolarkiewicz, 1989: Gravity waves, compensating subsidence and detrainment around cumulus clouds. *J. Atmos. Sci.*, **46**, 740–759.
- Brown, R. G., and C. S. Bretherton, 1995: Tropical wave instabilities: Convective interaction with dynamics using the Emanuel convective parameterization. *J. Atmos. Sci.*, **52**, 67–82.
- Chang, C. P., and H. Lim, 1988: Kelvin wave–CISK: A possible mechanism for the 30–50-day oscillations. *J. Atmos. Sci.*, **45**, 1709–1720.
- Chao, W. C., and L. Deng, 1998: Tropical intraseasonal oscillation, super cloud clusters, and cumulus convection schemes. Part II: 3D aquaplanet simulations. *J. Atmos. Sci.*, **55**, 690–709.
- Derbyshire, S. H., I. Beau, P. Bechtold, J. Y. Grandpeix, J. M. Piriou, J. L. Redelsperger, and P. Soares, 2004: Sensitivity of moist convection to environmental humidity. *Quart. J. Roy. Meteor. Soc.*, **130**, 3055–3080.
- Emanuel, K. A., 1987: An air–sea interaction model of intraseasonal oscillations in the Tropics. *J. Atmos. Sci.*, **44**, 2324–2340.
- , 1991: A scheme for representing cumulus convection in large-scale models. *J. Atmos. Sci.*, **48**, 2313–2335.
- Flatau, M., P. J. Flatau, P. Phoebus, and P. P. Niiler, 1997: The feedback between equatorial convection and local radiative and evaporative processes: The implications for intraseasonal oscillations. *J. Atmos. Sci.*, **54**, 2373–2386.
- Fu, X., and B. Wang, 2004: Differences of boreal summer intraseasonal oscillations simulated in an atmosphere–ocean coupled model and an atmosphere-only model. *J. Climate*, **17**, 1263–1271.
- Grabowski, W. W., 2000: Cloud microphysics and the tropical climate: Cloud-resolving model perspective. *J. Climate*, **13**, 2306–2322.
- , 2001: Coupling cloud processes with the large-scale dynamics using the Cloud-Resolving Convection Parameterization (CRCP). *J. Atmos. Sci.*, **58**, 978–997.
- , 2003a: MJO-like coherent structures: Sensitivity simulations using the Cloud-Resolving Convection Parameterization (CRCP). *J. Atmos. Sci.*, **60**, 847–864.
- , 2003b: Impact of cloud microphysics on convective–radiative quasi-equilibrium revealed by Cloud-Resolving Convection Parameterization (CRCP). *J. Climate*, **16**, 3463–3475.
- , 2004: An improved framework for superparameterization. *J. Atmos. Sci.*, **61**, 1940–1952.
- , and P. K. Smolarkiewicz, 1999: CRCP: A Cloud Resolving Convection Parameterization for modeling the tropical convecting atmosphere. *Physica D*, **133**, 171–178.
- , and M. W. Moncrieff, 2001: Large-scale organization of tropical convection in two-dimensional explicit numerical simulations. *Quart. J. Roy. Meteor. Soc.*, **127**, 445–468.
- , and —, 2002: Large-scale organization of tropical convection in two-dimensional explicit numerical simulations: Effects of interactive radiation. *Quart. J. Roy. Meteor. Soc.*, **128**, 2349–2375.
- , and P. K. Smolarkiewicz, 2002: A multiscale anelastic model for meteorological research. *Mon. Wea. Rev.*, **130**, 939–956.
- , and M. W. Moncrieff, 2004: Moisture–convection feedback in the Tropics. *Quart. J. Roy. Meteor. Soc.*, **130**, 3081–3104.
- , J.-I. Yano, and M. W. Moncrieff, 2000: Cloud-resolving modeling of tropical circulations driven by large-scale SST gradients. *J. Atmos. Sci.*, **57**, 2022–2039.
- Held, I. M., R. S. Hemler, and V. Ramaswamy, 1993: Radiative–convective equilibrium with explicit two-dimensional moist convection. *J. Atmos. Sci.*, **50**, 3909–3927.
- Hendon, H. H., 2000: Impact of air–sea coupling on the Madden–Julian Oscillation in a general circulation model. *J. Atmos. Sci.*, **57**, 3939–3952.
- Inness, P. M., and J. M. Slingo, 2003: Simulation of the Madden–Julian Oscillation in a coupled general circulation model. Part I: Comparison with observations and an atmosphere-only GCM. *J. Climate*, **16**, 345–364.
- Khairoutdinov, M. F., D. A. Randall, and C. DeMotte, 2005: Simulations of the atmospheric general circulation using a cloud-resolving model as a super-parameterization of physical processes. *J. Atmos. Sci.*, **62**, 2136–2154.
- Kiehl, J. T., J. J. Hack, and B. P. Briegleb, 1994: The simulated Earth radiation budget of the National Center for Atmospheric Research community climate model CCM2 and comparisons with the Earth Radiation Budget Experiment (ERBE). *J. Geophys. Res.*, **99**, 20 815–20 827.
- Lau, K.-M., L. Ping, C. H. Sui, and T. Nakazawa, 1989: Dynamics of super cloud clusters, westerly wind bursts, 30–60 day oscillations and ENSO: A unified view. *J. Meteor. Soc. Japan*, **67**, 205–219.
- Lin, J.-L., and Coauthors, 2006: Tropical intraseasonal variability in 14 IPCC AR4 Climate Models. Part I: Convective signals. *J. Climate*, **19**, 2665–2690.
- Lin, X., and R. H. Johnson, 1996: Kinematic and thermodynamic characteristics of the flow over the western Pacific warm pool during TOGA COARE. *J. Atmos. Sci.*, **53**, 695–715.
- Lindzen, R. S., 1974: Wave–CISK in tropics. *J. Atmos. Sci.*, **31**, 156–179.
- Madden, R., and P. R. Julian, 1971: Detection of a 40–50-day

- oscillation in the zonal wind in the tropical Pacific. *J. Atmos. Sci.*, **28**, 702–708.
- , and —, 1994: Observations of the 40–50-day tropical oscillation—A review. *Mon. Wea. Rev.*, **122**, 814–837.
- Majda, A. J., and M. G. Shefter, 2001: Models for stratiform instability and convectively coupled waves. *J. Atmos. Sci.*, **58**, 1567–1584.
- Maloney, E. D., and A. H. Sobel, 2004: Surface fluxes and ocean coupling in the tropical intraseasonal oscillation. *J. Climate*, **17**, 4368–4386.
- Mapes, B. E., 1993: Gregarious tropical convection. *J. Atmos. Sci.*, **50**, 2026–2037.
- , 1998: The large-scale part of tropical mesoscale convective system circulations: A linear vertical spectral band model. *J. Meteor. Soc. Japan*, **76**, 29–55.
- McFarquhar, G. M., and A. J. Heymsfield, 1997: Parameterization of tropical cirrus ice crystal size distributions and implications for radiative transfer: Results from CEPEX. *J. Atmos. Sci.*, **54**, 2187–2200.
- Moncrieff, M. W., 2004: Analytic representation of the large-scale organization of tropical convection. *J. Atmos. Sci.*, **61**, 1521–1538.
- Neelin, J. D., I. M. Held, and K. H. Cook, 1987: Evaporation–wind feedback and low-frequency variability in the tropical atmosphere. *J. Atmos. Sci.*, **44**, 2341–2348.
- Nilsson, J., and K. A. Emanuel, 1999: Equilibrium atmospheres of a two-column radiative-convective model. *Quart. J. Roy. Meteor. Soc.*, **125**, 2239–2264.
- Oouchi, K., 1999: Hierarchical organization of super cloud cluster caused by WISHE, convectively induced gravity waves and cold pool. *J. Meteor. Soc. Japan*, **77**, 907–927.
- Pierrehumbert, R. T., 1995: Thermostats, radiator fins, and the local runaway greenhouse. *J. Atmos. Sci.*, **52**, 1784–1806.
- Raymond, D. J., 2000a: The Hadley circulation as a radiative–convective instability. *J. Atmos. Sci.*, **57**, 1286–1297.
- , 2000b: Thermodynamic control of tropical rainfall. *Quart. J. Roy. Meteor. Soc.*, **126**, 889–898.
- , 2001: A new model of the Madden–Julian Oscillation. *J. Atmos. Sci.*, **58**, 2807–2819.
- , and X. Zeng, 2000: Instability and large-scale circulations in a two-column model of the tropical troposphere. *Quart. J. Roy. Meteor. Soc.*, **126**, 3117–3135.
- Slingo, J., and Coauthors, 1996: Intraseasonal oscillations in 15 atmospheric general circulation models: Results from an AMIP diagnostic subproject. *Climate Dyn.*, **12**, 325–357.
- Smolarkiewicz, P. K., L. G. Margolin, and A. Wyszogrodzki, 2001: A class of nonhydrostatic global models. *J. Atmos. Sci.*, **58**, 349–364.
- Sperber, K. R., J. M. Slingo, P. M. Innes, and W. K.-M. Lau, 1997: On the maintenance and initiation of the intraseasonal oscillation in the NCEP/NCAR reanalysis and in the GLA and UKMO AMIP simulations. *Climate Dyn.*, **13**, 769–795.
- Stephens, G. L., P. J. Webster, R. H. Johnson, R. Engelen, and T. L’Ecuyer, 2004: Observational evidence for the mutual regulation of the tropical hydrological cycle and tropical sea surface temperatures. *J. Climate*, **17**, 2213–2224.
- Tompkins, A. M., 2001a: Organization of tropical convection in low vertical wind shears: The role of water vapor. *J. Atmos. Sci.*, **58**, 529–545.
- , 2001b: On the relationship between tropical convection and sea surface temperature. *J. Climate*, **14**, 633–637.
- Waliser, D. E., K. M. Lau, and J.-H. Kim, 1999: The influence of coupled sea surface temperatures on the Madden–Julian Oscillation: A model perturbation experiment. *J. Atmos. Sci.*, **56**, 333–358.
- Webster, P. J., and R. Lukas, 1992: TOGA COARE: The Coupled Ocean–Atmosphere Response Experiment. *Bull. Amer. Meteor. Soc.*, **73**, 1377–1416.
- Weller, R. A., and S. P. Anderson, 1996: Surface meteorology and air–sea fluxes in the western equatorial Pacific warm pool during the TOGA Coupled Ocean–Atmosphere Response Experiment. *J. Climate*, **9**, 1959–1990.
- Wheeler, M., and G. N. Kiladis, 1999: Convectively coupled equatorial waves: Analysis of clouds and temperature in the wave-number-frequency domain. *J. Atmos. Sci.*, **56**, 374–399.
- , —, and P. J. Webster, 2000: Large-scale dynamical fields associated with convectively coupled equatorial waves. *J. Atmos. Sci.*, **57**, 613–640.
- Woolnough, J. S., J. M. Slingo, and B. J. Hoskins, 2000: The relationship between convection and sea surface temperature on intraseasonal timescale. *J. Climate*, **13**, 2086–2104.
- , —, and —, 2001: The organization of tropical convection by intraseasonal sea surface anomalies. *Quart. J. Roy. Meteor. Soc.*, **127**, 887–907.
- Wu, X., W. W. Grabowski, and M. W. Moncrieff, 1998: Long-term behavior of cloud systems in TOGA COARE and their interactions with radiative and surface processes. Part I: Two-dimensional modeling study. *J. Atmos. Sci.*, **55**, 2693–2714.
- , W. D. Hall, W. W. Grabowski, M. W. Moncrieff, W. D. Collins, and J. T. Kiehl, 1999: Long-term behavior of cloud systems in TOGA COARE and their interactions with radiative and surface processes. Part II: Effects of cloud microphysics on cloud–radiation interaction. *J. Atmos. Sci.*, **56**, 3177–3195.
- Zhang, C., 2005: Madden-Julian oscillation. *Rev. Geophys.*, **43**, RG2003, doi:10.1029/2004RG000158.
- Zheng, Y., D. E. Waliser, W. F. Stern, and C. Jones, 2004: The role of coupled sea surface temperatures in the simulation of the tropical intraseasonal oscillation. *J. Climate*, **17**, 4109–4134.